



# Wake characteristics in high solidity horizontal axis hydrokinetic turbines: a comparative study between experimental techniques and numerical simulations

Marianela Machuca Macías<sup>1</sup> · Rafael C. F. Mendes<sup>2</sup> · Michael Pereira<sup>3</sup> · Ivan Dobrev<sup>3</sup> · Taygoara F. Oliveira<sup>2</sup> · Antonio C. P. Brasil Junior<sup>2</sup>

Received: 6 March 2023 / Accepted: 6 November 2023 / Published online: 14 December 2023  
© The Author(s), under exclusive licence to The Brazilian Society of Mechanical Sciences and Engineering 2023

## Abstract

Hydrokinetic turbines utilizing renewable energy from water streams, such as tidal or river currents, offer a sustainable solution for electricity generation in remote coastal or fluvial regions. While there has been extensive research on the wake characteristics of low-solidity turbines, studies focusing on high-solidity turbines are limited. This study aims to address this research gap by characterizing the turbulent wake of a high-solidity, four-bladed hydrokinetic turbine using a combination of experimental and numerical approaches. Experimental investigations are conducted in two wind tunnel facilities, employing particle image velocimetry and hot-wire anemometry to measure and identify flow structures in the near-wake region. Additionally, the applicability of the actuator line method for high-solidity turbines is validated, considering the challenges posed by the higher blockage effect associated with such turbines. Numerical simulations are performed using an unsteady Reynolds-averaged Navier–Stokes approach, incorporating a full-geometry model of the rotating rotor and employing the actuator line concept for simplified modeling. The findings from this study provide valuable insights into the wake characteristics of high-solidity hydrokinetic turbines, contributing to the understanding of their performance and environmental implications.

**Keywords** Hydrokinetic turbines · High solidity · Actuator line method · PIV · Hot-wire measurements · CFD

---

Technical Editor: Erick Franklin.

---

✉ Marianela Machuca Macías  
marianela.machuca@uca.es

Rafael C. F. Mendes  
rafael.mendes@unb.br

Michael Pereira  
michael.pereira@ensam.eu

<sup>1</sup> Departamento de Ingeniería Mecánica y Diseño Industrial, Escuela Superior de Ingeniería, Universidad de Cádiz, Puerto Real 11519, Spain

<sup>2</sup> Laboratory of Energy and Environment, Department of Mechanical Engineering, Faculty of Technology, University of Brasilia, 70910-900 Brasilia, DF, Brazil

<sup>3</sup> ENSAM - Ecole Nationale d'Arts et Métiers. Lab. DynFluid, 151, Bd. de l'Hôpital, 75013 Paris, France

## 1 Introduction

Nowadays, the renewable source of energy issued from water streams (tidal or river currents) is an alternative way to provide electricity for remote coastal or fluvial regions with local communitarian needs. Small- and medium-sized turbines can be used as a good solution for renewable and sustainable electricity production, employing hydrokinetic energy conversion devices with low environmental impacts [1, 2].

The characterization of the water flow, the understanding of the physical mechanisms of energy conversion, and hydrodynamics of horizontal-axis hydrokinetic turbines compose an important background to estimate the performance of the machines and also to verify how disturbed flow may impact the surroundings of the turbine installation and its environment. Therefore, the characterization of the turbulent wake is an important step for the entire evaluation of the operation of a hydrokinetic installation.

The wake is the downstream flow region formed by the interaction between the free flow and rotor blades. It exhibits high crossflow and spanwise vorticity, velocity deficit, and elevated turbulence levels [3]. Vortex structures play a significant role, influencing shape, hydrodynamics, and turbulent kinetic energy downstream. The near-wake region, within approximately 2.0–4.0 rotor diameters downstream, features strong hydrodynamic conversion, counter-rotating tip vortices, and hub vortices [4]. In the far-wake region, large structures dissipate, pressure recovers, and turbulence intensity decreases. Various numerical and experimental techniques are employed to study wake characteristics in horizontal-axis turbines [5].

In experimental studies, turbines are tested in water flumes [6] or wind tunnels [7] facilities to achieve a wide range of operational points. Tests are commonly equipped with a velocity-based measuring method, such as PIV [8], hot-wire [9], or laser Doppler anemometers [10], in order to define the length and other parameters of turbulence inside the wake [11].

For estimation of the performance of the full hydrokinetic turbine, an experimental methodology based on small-scale tests in the wind tunnel facility was carried out. The approach developed by Macias et al. [7] is presented as an alternative to the experimental evaluation of hydrokinetic turbines, which is generally based on experiments in laboratory water flumes. The use of wind tunnel experiments was supplemented by a model-to-prototype extrapolation approach in which the performance results of the small-scale airflow experiments are transposed to the prototype real scale in water flow. This is achieved through a calibrated methodology using some arguments of blade element momentum theory. The works of Macias et al. [7] and Nunes et al. [12] present a successful validation of the upscaling approach by numerical simulations (CFD) at both scaling levels and by experimental data.

On the other hand, numerical analysis plays a crucial role in describing wake structures, with CFD simulations being a primary tool. There are various methods to evaluate turbines in CFD, such as using the full rotor geometry [13], or modeling the wake behavior using techniques such as the actuator disk [14], actuator line method [15], and actuator surface method [16]. The primary differences between these methods are related to their computational cost and the level of detail they can provide in the results. While the full-geometry method can produce more detailed flow characteristics, it requires much longer simulation times.

Alternatively, the actuator line method can be a useful solution to describe the wake with accurate results and less computation effort, as demonstrated in recent studies [17–19]. The actuator line method ALM combines the blade element momentum (BEM) methodology with the Navier–Stokes equations computing the forces on the turbine and the

flow around the rotor. The crucial issue is that the method does not require surface meshing or the resolution of the detailed flow in the boundary layer because the blades are discretized in actuator lines formed by points. In the literature, there are studies using unsteady Reynolds-averaged Navier–Stokes (URANS) approaches [20, 21] and large-eddy simulations (LES) [22, 23], as well as works dedicated to the study of hydrokinetic arrangements with the objective of characterizing the wake and optimizing the positioning of an array of machines [24, 25], and studies using turbines with diffuser [26].

The identification of physical features in the wake flow of horizontal-axis turbines has been extensively studied and documented through numerous previous research efforts, concerning the fluid flow through based on wind turbines or large hydrokinetic turbines with small solidity (e.g., [27–32]), where the blockage effect is smaller, due to the geometry of the rotor with three sparse blades and often with a low rotational speed. Recently, several studies have focused on characterizing the wake of high-solidity turbines, particularly in the context of ducted turbines (e.g., [33–35]). However, research specifically investigating the wake characteristics of high-solidity turbines without ducts remains limited, which are typically found in small hydrokinetic turbine cases. Therefore, it is crucial to consider the differences that high solidity can cause, such as a higher blockage effect, in the analysis of wake behavior.

This paper aims to characterize the wake flow from a high-solidity, four-bladed hydrokinetic turbine, as shown in Fig. 1, employing different experimental and numerical approaches. Experiments utilize a small-scale turbine in two wind tunnel facilities to measure and identify the flow structures at the near-wake region with two different approaches, i.e., particle image velocimetry (PIV) and hot-wire anemometry. Additionally, another objective of this study is to validate the applicability of the actuator line method for high-solidity turbines, as this method is commonly employed for low-solidity rotors. Numerical simulations are conducted using an unsteady Reynolds-averaged Navier–Stokes (RANS) approach, encompassing the complete 3D rotating rotor formulation (full geometry), along with the implementation of the actuator line concept for simplified modeling.

The organization of this paper is as follows. Section 2 presents the high-solidity hydrokinetic turbine employed in this study providing an overview of the main non-dimensional parameters involved in the investigation. Section 3 outlines the proposed experimental methodology, including the small-scale turbine description, the wind tunnel facilities, and the conducted experimental tests. Section 4 includes details on the CFD simulations used for numerical studies. In Sect. 5, the results obtained from the experimental tests and numerical simulations are compared and discussed.

**Fig. 1** Main flow structures at high-solidity hydrokinetic turbine HK10

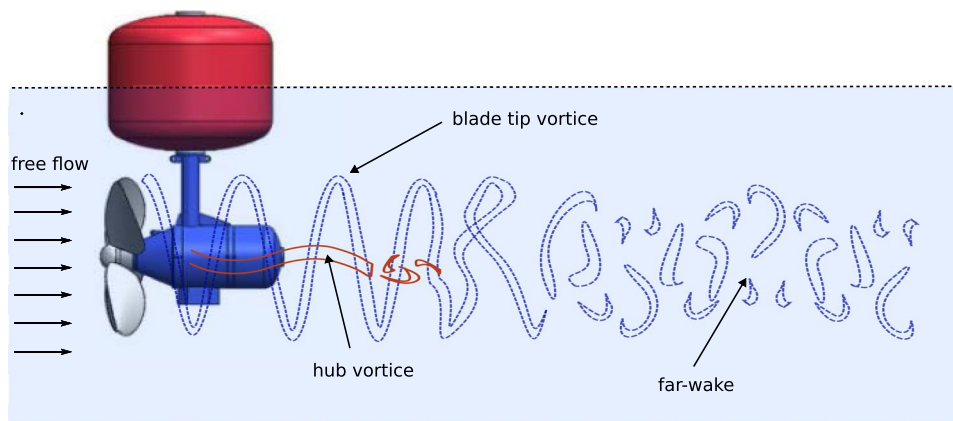


**Table 1** HK10 turbine design and operation features

Diameter ( $D$ )	2.2 m	Blade profile	NACA4415
Nominal power ( $P_n$ )	10 kW	Generator	Permanent magnets with axial flow
Free flow velocity ( $U_0$ )	2.5 m/s	Transmission	1:12 multiplication. Planetary gears
Chord length ( $c$ )	0.41 m	Power regulation	AC/DC rectification with converter
Nominal rotation	35 rpm	Nominal voltage	120/240/380 V

Finally, Sect. 6 summarizes the conclusions drawn from this study.

## 2 High-solidity hydrokinetic turbine

In the present study, the high-solidity, four-bladed HK10 turbine is considered as shown in Figs. 1 and 2. The rotor was developed in R&D Brazilian cooperation involving the University of Brasilia and the AES-Tiete company. With 2.2 m diameter and NACA4415 hydrodynamic profile to blade design, this machine has a rated power of 10 kW and operates at a water speed of 2.5 m/s (see [36], for instance). It was designed to convert the kinetic energy of water streams, close to the free surface, by means of a floating integrated electromechanical device. The description of the wake flow is important to establish an array configuration of several machines working together and also to evaluate the region affected by the turbine that can impact the surrounding environment.

Table 1 summarizes generic technical information about the turbine employed in this study. Besides, Table 2 presents blade profile descriptions in detail: axial distance, chord, and torsion angle.

In this study, a comparison between experimental and numerical methodologies is provided to investigate the high-solidity hydrokinetic turbine HK10 wake. Besides, the power conversion efficiency  $C_p$  is computed for various operating regimes defined by the tip speed ratio TSR. The non-dimensional parameters are described by

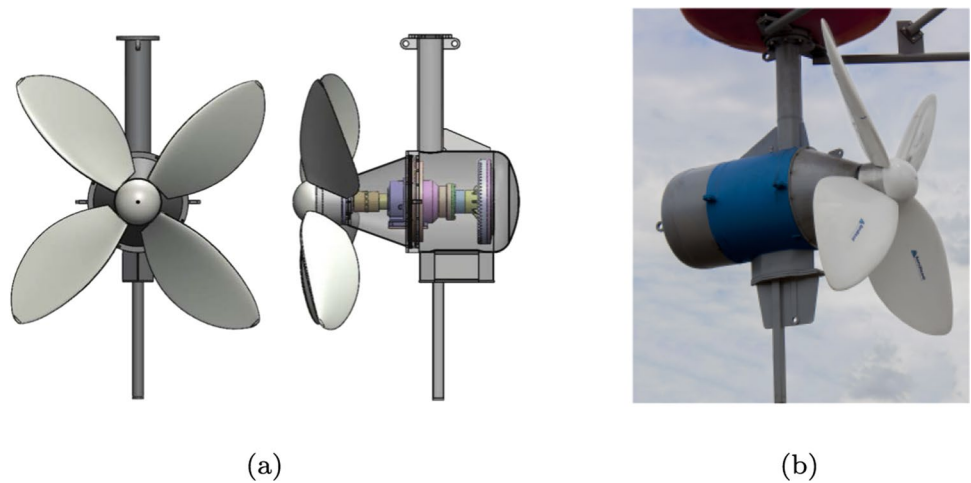
**Table 2** HK10 rotor geometry information along the blade: radial distribution, chord, and twist angle

Radial distance (m)	Chord (m)	Twist angle ( $^\circ$ )
0.150	0.29	-43.69
0.218	0.38	-40.68
0.286	0.44	-37.86
0.354	0.49	-35.22
0.421	0.52	-32.73
0.489	0.53	-30.41
0.557	0.54	-28.43
0.625	0.53	-26.19
0.693	0.50	-24.29
0.761	0.47	-22.52
0.829	0.43	-20.87
0.896	0.38	-19.37
0.964	0.31	-17.90
1.032	0.22	-16.57
1.100	0.01	-15.34

$$C_p = \frac{\omega T}{\frac{1}{2} \rho A U_0^3}, \tag{1}$$

$$TSR = \frac{\omega R}{U_0}. \tag{2}$$

**Fig. 2** HK10 turbine: **a** front and lateral views of conception model; **b** field assembly



being the free flow velocity  $U_0$ , the density  $\rho$ , the torque  $T$ , the rotation speed  $\omega$ , and the radius  $R$ . The area swept by the rotor is defined by  $A = \pi R^2$ .

The rotor solidity  $\sigma$  refers to the ratio of the blade projections and the swept area of the turbine, where  $N_b$  is the number of blades,  $H_r$  is the hub radius, and  $c_r$  is the chord at radial distance  $r$ .

$$\sigma = \frac{\int_{H_r}^R N_b c_r dr}{\pi R^2}. \tag{3}$$

Rotors with high solidity carry a lot of material, and the flow hydrodynamic of the blades can interfere with neighboring blades. Table 3 lists the main parameters to estimate the solidity rotor for HK10 and other low-solidity horizontal-axial turbines in the literature.

### 3 Experimental approach

Two wind tunnel experiments were carried out in the present study. The characterization of the wake flow and the performance of the hydrokinetic turbine HK10 has been developed in a framework of an experimental international collaboration involving the University of Brasilia (UnB), in Brazil, and the Ecole Nationale d'Arts et Métiers (ENSAM-Paris), in France, to design and evaluate the small hydrokinetic turbines for remote communities.

Experimental tests were conducted on a small-scale turbine, analyzing the wake flow using particle image velocimetry (PIV) and computing the characteristic curves  $C_p \times TSR$  through the torque and rotational velocity measurements. The small-scale curve performance was scaled up obtaining the characteristic curves of the full-scale hydrokinetic turbine employing the upscaling approach developed by Macias et al. [7], as also reported by Nunes et al. [12] to HK10 turbine. Subsequently, computational fluid dynamics (CFD) simulations were carried out on the full-size turbine to validate the flow

**Table 3** Solidity rotor value estimation for horizontal-axial turbines

Turbine type	HK10 Hydrokinetic	Tucunaré [7] Hydrokinetic	NREL Phase VI [37] Wind
$N_b$	4	3	2
$c$ (m)	0.41	0.828	0.542
$D$ (m)	2.2	5.0	5.029
Solidity $\sigma$	0.475	0.150	0.070

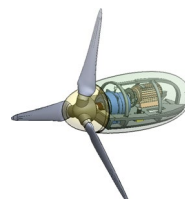
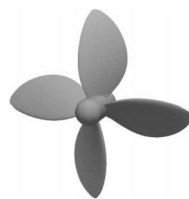


Photo from Lee Jay Fingersh, NREL 11587

measurements obtained in the wind tunnel and to verify the upscaling method based on the experimental results.

### 3.1 Small-scale turbine

The experimental study was conducted on a small-scale turbine model of 1:10th of real dimensions. The four-blade model is manufactured in an ABL 3D printer system and finished with epoxy paint (Fig. 3). The same blade profile (NACA 4415) was employed in small-scale and full-size turbines to keep the geometric similarity between both machines.

The kinematic similarity is ensured by the same velocity triangles in the inflow of the blade section, and consequently, the same values of  $TSR$  in both scales must be guaranteed. Finally, the dynamic similarity is not achieved for any regime operation because the Reynolds numbers are overly different due to differences in the complex phenomena over the turbine blades such as transition laminar-turbulent and boundary layer detachment. The Reynolds numbers based on the rotor diameter  $Re_D$  were computed such as  $1.8 \times 10^5$  and  $5.5 \times 10^6$ , to model and full size, respectively. To address the discrepancy between Reynolds numbers and achieve scaling of results from small- to full-scale turbines, an empirical power law from [7] has been applied. This power law serves to correct the lack of dynamic similarity in  $C_p$  (power coefficient) results and enables a more accurate comparison between different scales. The power law was obtained relating the power coefficients and the Reynolds numbers for the model in the wind tunnel and full-scale hydrokinetic turbine by means of BEM theory equations. Table 4 summarizes the main parameters of the full-scale and model turbines.

**Table 4** Full-size and small-scale turbine parameters

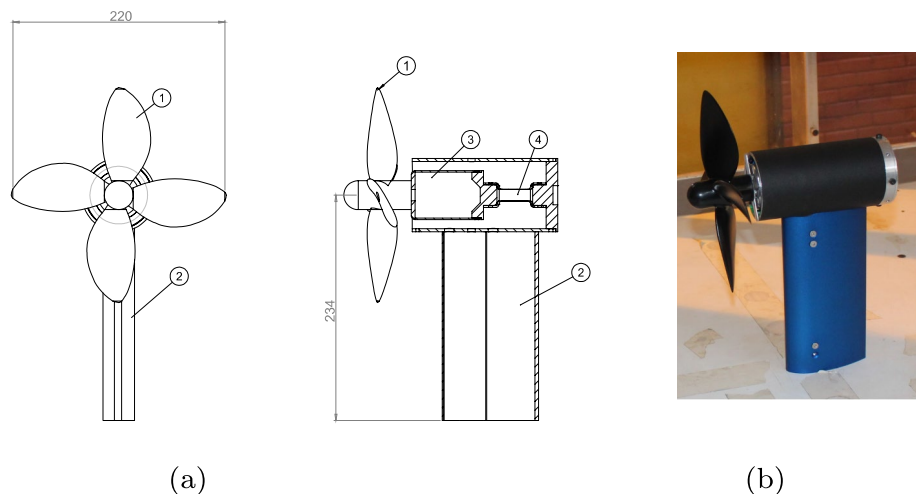
Turbine type	Full-size Hydrokinetic	Small-scale Wind
Fluid	Water	Air
Free flow velocity (m/s)	2.5	12
Diameter (m)	2.2	0.22
Chord length (m)	0.41	0.041
Nominal rotation (rpm)	35	1698
Nominal TSR	1.6	1.6
$Re_D$	$5.5 \times 10^6$	$1.8 \times 10^5$

### 3.2 Wind tunnel facilities

The first group of experiments was performed in the open-loop wind tunnel of the Energy and Environment Laboratory of the University of Brasília. This tunnel has a test section of  $1.2 \text{ m} \times 1.2 \text{ m}$  with a length of 2.0 m. With a contraction ratio of 8:1 and an axial fan of 10 kW, this wind tunnel can reach a controlled airspeed of up to 20 m/s, with a turbulence intensity of less than 0.2%. Figure 4 illustrates a general overview of the test facility. A Pitot tube is used to measure the free flow velocity, and the air temperature and relative humidity are monitored with calibrated electronic sensors. The experimental uncertainty of the velocity measurements is  $\pm 0.1 \text{ m/s}$ .

The small-scale 1:10 turbine model is placed in the center of the test section as shown in Fig. 3. The experiments to obtain the performance curves are carried out using a torsional torque meter load cell with a small electrical generator as a break. The system maintains the operation of the turbine runner at a constant rotational speed, where an adjusted electronic resistive load through a PWM-PID control system dynamically dissipates the converted electricity power.

**Fig. 3** **a** Small-scale turbine scheme (dimensions in mm): (1) runner; (2) tower; (3) permanent-magnet generator; (4) torsional load sensor. **b** The 1:10 small-scale turbine inside the wind tunnel test section



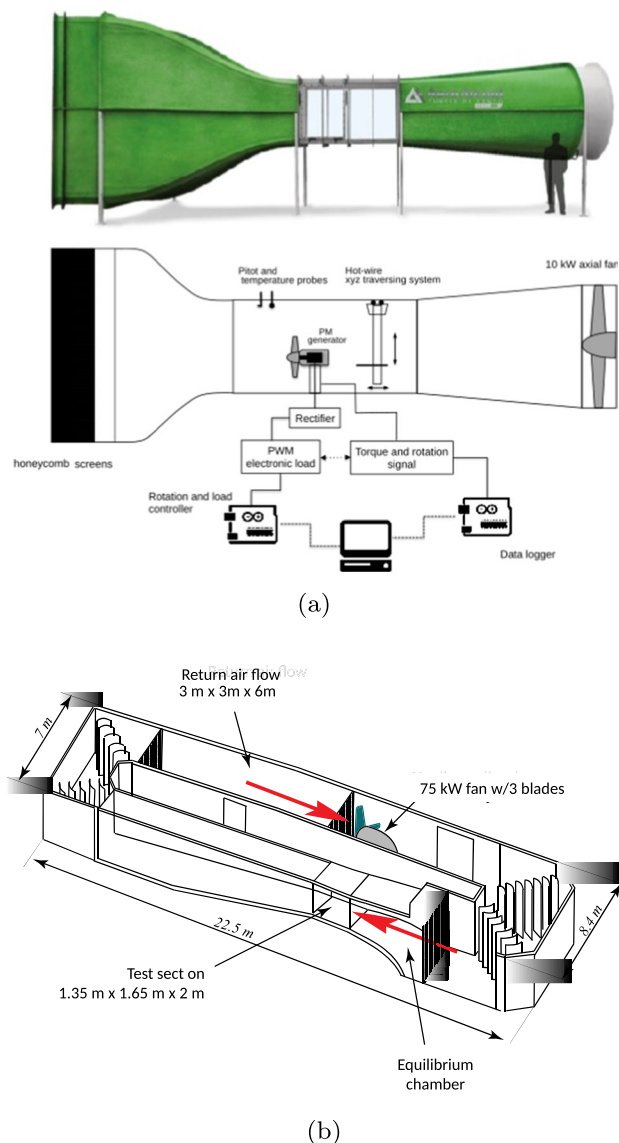


**Fig. 4** Wind tunnel facilities: **a** University of Brasilia open-loop and **b** ENSAM-Paris closed-loop

A closed-loop PID control system achieves stable rotation for a given wind speed by using electronically controlled settings for the generator load levels, with the accuracy of torque measurements by a torsional load cell equal to  $10^{-4}$  N m. The operation of the turbine model keeps the rotation,  $N$ , constant at a fixed value within  $\pm 10$  rpm fluctuations in the range of 300–2500 rpm (measured by an optical infrared rotation sensor). For a fixed wind tunnel velocity (around 12 m/s), a performance curve can be automatically obtained by the programmable control system, which covers the required range of rotational speed, measuring and registering the torque and the rotation by the data-logger.

In this facility, a 3D transverse system displaces the hot-wire probe for all positions in the test section (see Fig. 4a).

A DANTEC system with MiniCTA 54T40 with probe 55P01 is employed. It allows the measurement of the wake profiles of one component mean velocity and turbulence intensity.

The second wind tunnel facility is in the Laboratory of Fluid Engineering and Energy Systems of ENSAM Paris (Fig. 4b). It is a closed-loop installation where the test section is open to atmospheric pressure (Prandtl-like tunnel). The test section has dimensions of  $1.35 \text{ m} \times 1.65 \text{ m}$  with a 2 m length. The contraction of 1:12 ensures homogeneous and low turbulence with an airflow velocity of up to 40 m/s. The velocity measurement with the PIV system can be carried out properly inside the open test section. All wind tunnel controls and airflow conditions are registered with accuracy for the velocity of  $\pm 0.1 \text{ m/s}$ .

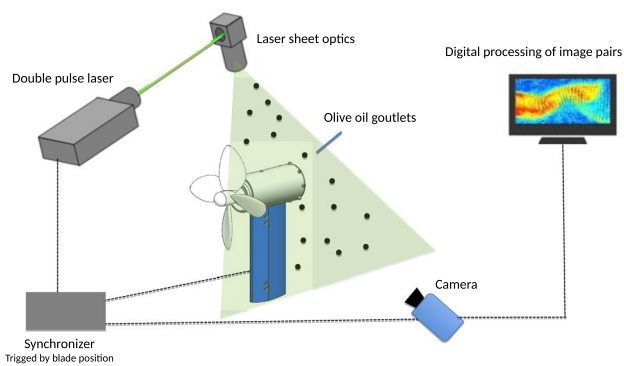
The PIV characterization of the turbine wake is obtained by 2D measurements using a synchronization triggered by the angular position of the blade. In this approach, each set of particle image pairs (olive oil microdrops) registers the flow field at one angular position, allowing scanning of the mean wake flow for the entire rotor (see [38], for instance).

Finally, in the present experimental campaign, the turbine model was tested in the UnB facility, obtaining the performance curve ( $C_p \times \text{TSR}$ ) and horizontal profiles of mean axial velocity and turbulence intensity. After that, a PIV characterization of the wake was obtained in the facility of ENSAM, identifying the main vortice structures in the near-wake flow. All these experimental data are compared to a detailed simulation of the fluid flow (Fig. 5).

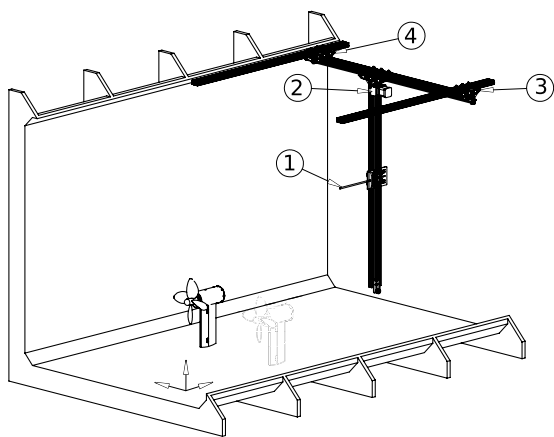
## 4 Numerical setup

Simulation of turbulent flow through the turbine rotor was performed using the platform ANSYS-CFX. The unsteady Reynolds-averaged approach (URANS) was used to describe the flow with time-dependent fields of velocity, pressure, and turbulence variables. This approach enables the analysis of the dynamic flow behavior, especially in the wake region, which is essential for characterization, particularly in wind turbine farms where the wake velocities and turbulence levels from upwind turbines serve as the incoming flow for downstream turbines [39, 40]. The turbulence model  $k-\omega/SST$  with transition version  $\gamma - Re_\theta - SST$ , also known as transition SST [41], was employed in two different subdomains: The first is a parallelepiped domain defining the large fluid region affected by the machine [42, 43]. The second is the submerged cylindrical domains containing the turbine rotor. This surrounding cylindrical volume rotates at the same speed as the turbine blades. Figure 6 shows both subdomains in a simplified schematic form, and this figure illustrates the boundary conditions employed in the simulations.

A 3D mesh with 5,572,162 nodes was generated by ANSYS-CFX/MESH, where tetrahedral elements in an



(a)



(b)

**Fig. 5** Velocity measurements setup: **a** PIV and **b** hot-wire anemometer system, where (1) probe and (2), (3), and (4) step motors to move the probe in the Cartesian plane

unstructured mesh were used with refinement in the wake and in the near-wall regions using the inflation approach, as shown in Figs. 7a and 8. The refinement near the wall guarantees small values for the average variable  $y_{ave}^+ = 1.6$ ,

which is an important condition for better results with the turbulence model.

Complementary, another group of CFD simulations was carried out using the actuator line method (ALM). It was performed using the OpenFOAM platform where the model of source terms in the Navier–Stokes equations has been changed to take into account the hydrodynamical influence of each blade section in the fluid flow. Hence, the four rotating actuator lines define the source terms formulated by the hydrodynamical forces (drag and lift) computed after the geometry of the blade (airfoil section, chord length, and assembly angle), taking into account the distance of each node of the mesh to the set of points, which represents the blade. The airfoil hydrodynamical coefficients are computed using XFOIL tool. Besides, in ALM simulations the hub/nacelle was modeled as an actuator cylinder. More details about the ALM process are given in Appendix.

For the ALM approach, the mesh is smaller than the Full 3D because it does not need the discretization of the blade surface and its near-wall gradients. The final mesh discretizes properly the wake region and has 4,000,000 nodes, as shown in Fig. 7b.

A previous mesh assessment was performed considering different dimensions and levels of refinement of the grids. Table 5 shows the mesh convergence study to full 3D simulations at normal setting rotor condition ( $\omega = 35 \text{ rpm}$  and  $U_0 = 2.5 \text{ m/s}$ , and consequently,  $TSR = 1.6$ ). All the tested mesh showed a similar  $C_p$ , varying less than %3 between coarse and fine mesh, where this value was validated in the experimental approach. Also, the refinement study proceeds until reaching an ideal  $y^+$  for applying the SST turbulence model [41]. The final meshes illustrated in Fig. 7 were selected for the condition where the  $C_p$  and  $y_{ave}^+$  values had attained the proper condition in the nominal setting for the rotor. Then, the ALM mesh was reproduced to keep the same element density in the near-wake region. In Table 6 is established a comparison between the simulation time

**Fig. 6** Scheme of CFD domain definitions and boundary conditions for full-geometry simulations

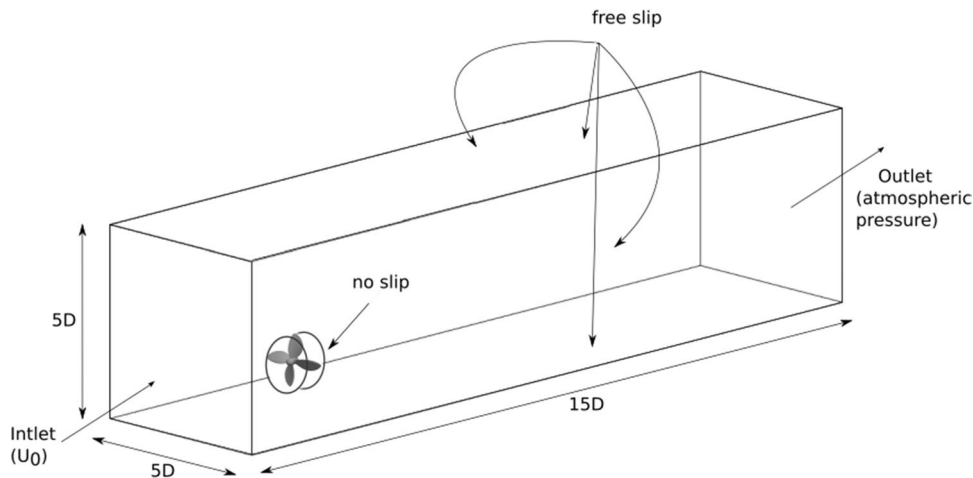


**Fig. 7** **a** CFD-Full 3D mesh with  $5.5 \times 10^6$  nodes; **b** CFD-ALM mesh with  $4 \times 10^6$  nodes

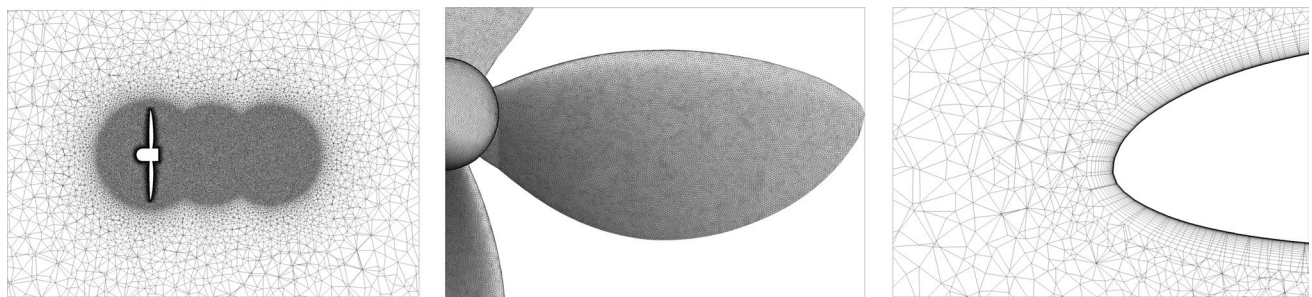
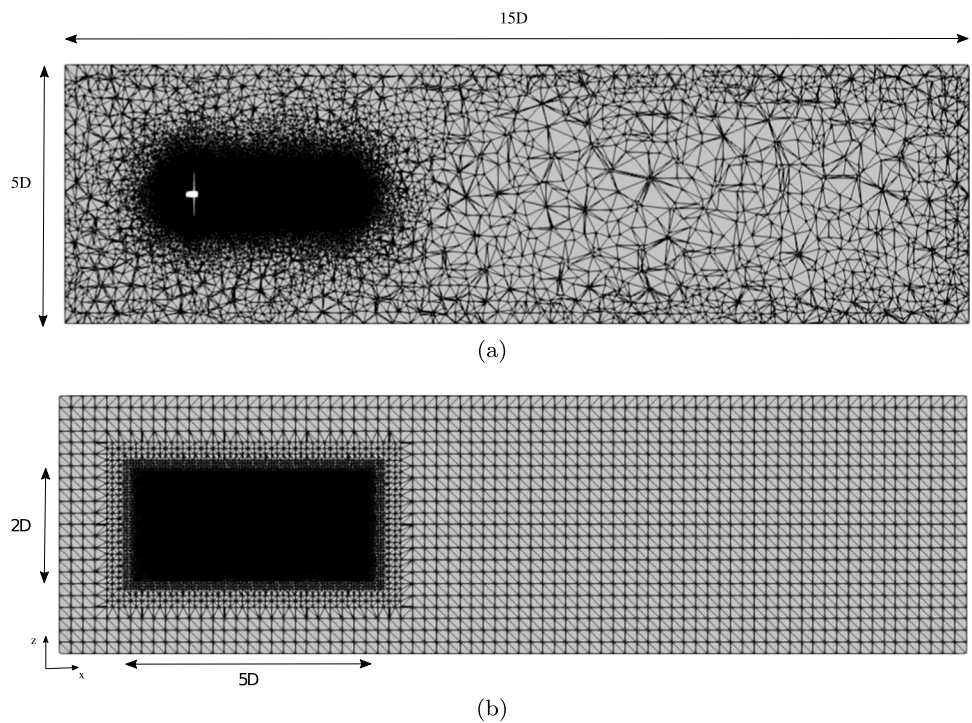


**Fig. 8** Mesh details for CFD-Full 3D simulations: near-wake refinement region, mesh on the blade surface, and prismatic elements modeling the boundary layer region

**Table 5** Mesh convergence study of the hydrokinetic rotor operating under the design conditions (TSR=1.6) in Full 3D simulations in Ansys-CFX

Grid levels	N° Nodes	$y_{ave}^+$	$C_p$
Coarse	$4.2 \times 10^5$	323.62	0.381
Medium	$1.2 \times 10^6$	117.77	0.386
Fine	$5.5 \times 10^6$	1.57	0.390

between the CFD-Full 3D and CFD-ALM methodologies. The residuals for all equations fall below  $1 \times 10^{-5}$ .

**Table 6** Simulation time comparison between the CFD-ALM and CFD-Full 3D methodologies

	N° Nodes	Core-hours/sec
CFD-Full 3D	$5.5 \times 10^6$	9000
CFD-ALM	$4.0 \times 10^6$	50

## 5 Results and discussion

### 5.1 Performance results

In Fig. 9, the performance results as the  $C_p \times TSR$  curve are presented. The wind tunnel experiment results for converted torsional power, corrected to the prototype scale,



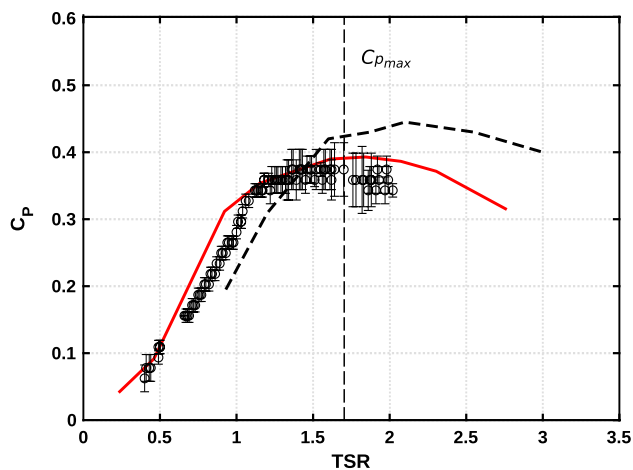


**Fig. 9** CFD simulations results. **a** Power coefficient for ALM approach, full-geometry CFD simulations, and experimental points from [36]. The maximum values of  $C_p$  are represented by the vertical dashed line

are superposed to the results of the CFD-Full 3D and the CFD-ALM approach simulations obtained for the water flow.

The results for the CFD-Full 3D simulations and experiments have a good agreement in the TSR range between 0.5 and 2.0. For higher values, the results of simulations using the ALM approach are not too precise compared to the experimental observations and full CFD. In that situation, the results of the actuator line, based on the integration of the aerodynamic forces through the lines (like in the BEM approach), have an inherent uncertainty related to the lift and drag coefficients computed by XFOIL. Hence, the result for the stalled flow on the blade surface, equivalent to TSR higher than 2.0, does not present a good quality for the  $C_p$  estimates. On the other hand, for the nominal value in the maximum position of the power coefficient, the performance is properly predicted.

It is observed that the designed propeller machine has a good performance with a maximum value around  $C_p = 0.39$ ,

occurring for  $TSR = 1.7$ . Values close to the maximum value of  $C_p$  occur, with a variation of  $\pm 6\%$ , in the range of  $TSR$  between 1.5 and 2.5. It is very useful to operate the machine close to its nominal condition, maintaining the conversion efficacy closest to the best value.

Finally, the performance results suggest that the parameters used in the CFD methodology are correct and the method can reproduce good results, especially close to the operating point. For this nominal condition, the analysis of the wake flow will be carried out.

## 5.2 Wake flow visualization

In Figs. 10, 11, and 12, the wake visualization from the PIV measurements and CFD simulations are shown by time-averaged velocity and vorticity during a turbine cycle. Figure 10b and c presents the near-wake flow visualization with a longitudinal mean velocity component. The dotted square in CFD-Full 3D and CFD-ALM figures highlights the tip vortex region to be compared with the PIV data details in Fig. 10a. The PIV data identify properly the tip vortices spaced to the distance equivalent to the  $U_0/f_{blade}$  where  $f_{blade}$  denotes the blade passage frequency. The presence of the three vortex cores for the PIV case and the CFD simulations can be recognized in the figures.

The near-wake vortex structures are also visualized from the numerical results for Full 3D and ALM (Fig. 11). The large structures associated with the tip vortices and the hub core shadowing are correctly described. In Fig. 11a, the blade tip vortex is observed as a helicoidal structure that appears in red color, located just after the rotor, resulting in the high angular velocities in this region. On the other hand, the hub/nacelle vortex with a cylindrical shape is located in the central zone of the near wake and appears in green/blue color, representing the low-speed zone influenced by the rotor nacelle. The two numerical methods present very similar results regarding the formation of the coherent structures of the wake.

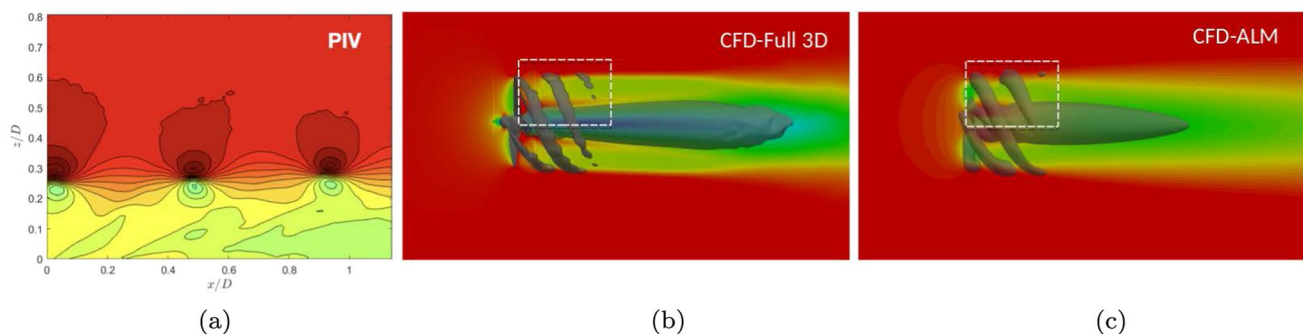


**Fig. 10** Near-wake flow visualization with longitudinal mean velocity component for **a** PIV data and for **b** CFD with Full 3D and **c** ALM

**Fig. 11** **a** Q-Criterion filter and **b** vorticity in the longitudinal plane (CFD-Full 3D and CFD-ALM simulations)

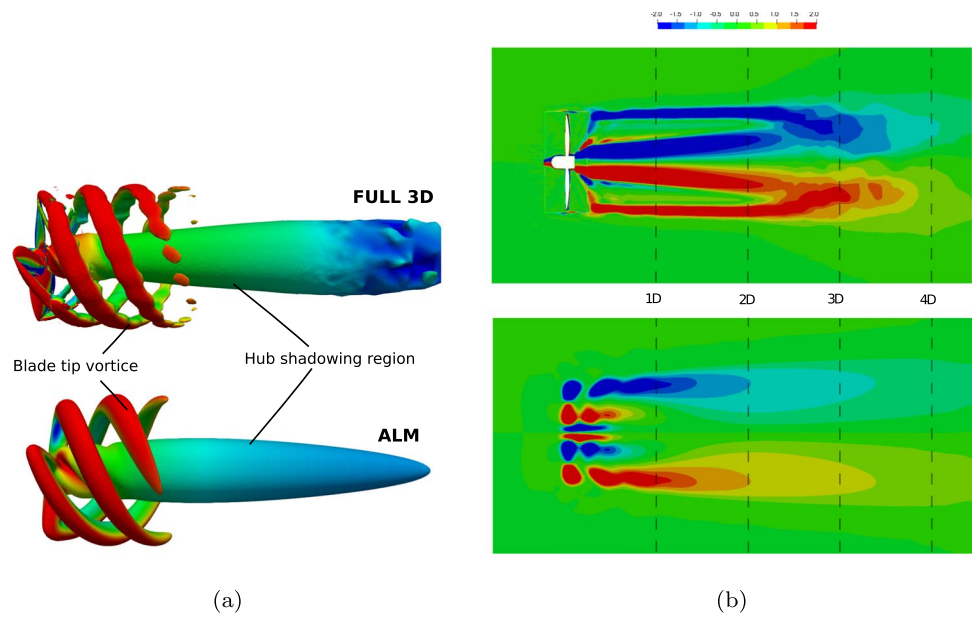


**Fig. 12** Mean velocity field  $U/U_0$  in the rotor transverse plane: **a** CFD-Full 3D; and **b** CFD-ALM; **c** Rotor downstream transverse planes at distance 1D, 2D, 3D, and 4D

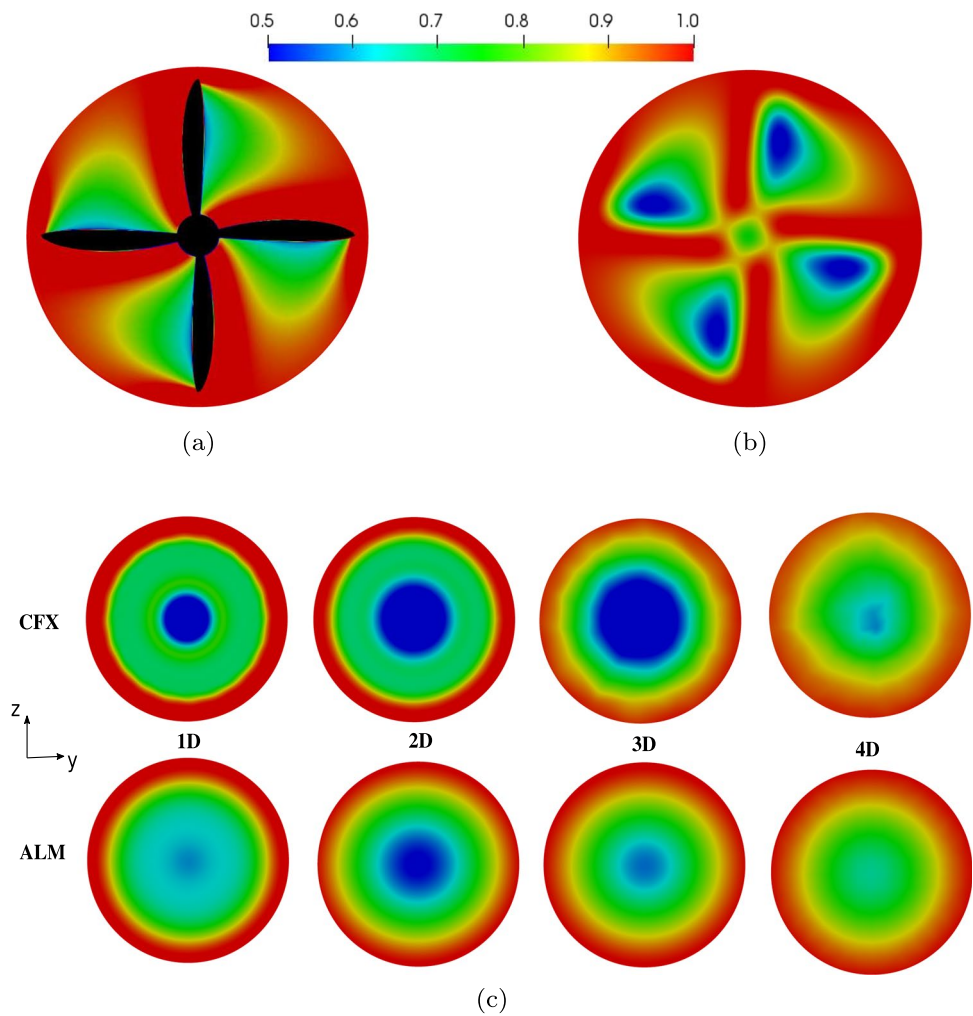


Figure 11b shows the dimensionless vorticity fields, also in the longitudinal midplane, for both numerical methods. It is observed how the results obtained by the ALM method also recover those extracted from the CFD-Full 3D, showing similar vorticity fields in morphology and intensity. The divergence between the figures is related to the presence of the hub/nacelle, which induces a zone of greater vorticity in the central line, where the root vortex occurs. The flow visualization suggests that for this turbine the near-wake region remains close to the  $x/D < 2.0-3.0$ , which is slightly different from the three-blade machines, for instance.

As mentioned, for the ALM simulation, the core region is smaller than the Full 3D simulation. It is difficult to describe the wake region near the center line by an effect of the blockage of the hub only considering the Navier–Stokes source terms. On the other hand, the main helicoidal structure of the vortices generated by the blade elements is properly obtained in computations, and both are compatible with the PIV data. The two modeling approaches can capture the destruction of this structure and as a consequence the end of the near-wake region. It is observed in Fig. 11, in particular in the levels of the vorticity in the rotor plane.

Bringing more information about the wake computed in the simulations, Fig. 12 presents cross-sectional planes of the rotor showing the velocity field from another perspective. In Fig. 12a and b, the mean velocity distribution in the rotor plane is observed, for both numerical simulations, with similar behavior. CFD-ALM simulation presents a lower velocity in the blade region due to the absence of blade geometry in the simplified method. Figure 12c displays the transverse planes of mean velocity at various distances downstream of the rotor. As mentioned previously, the main discrepancy between both methods is the lower velocity level in the near-wake central region, which appears more accentuated in the CFD-Full 3D case. Finally, at a 4D distance, it is observed that the maximum velocity deficit has been overcome.

### 5.3 Transversal profiles and rear mapping

In Fig. 13, the experimental data profiles of mean axial velocity and turbulence intensity are presented and compared to the CFD simulations in the region of near wake. Figure 13a presents the dimensionless mean velocity ( $U/U_0$ ) in different position rotor downstream ( $x/D = 1;2;3;4$ ) providing information about the wake evolution. The velocity profiles computed by CFD simulations show a good agreement in qualitative and quantitative terms. The main difference between the CFD results appears in the central region of the machine comprised by the interval  $|z/D| < 0.2$ , referring to the hub/nacelle of the turbine, due to the velocity deficit. That characteristic is accentuated in the closest rotor profile ( $x/D = 1$ ) and decreases along the wake. In addition, Fig. 13 presents the velocity profiles ( $x/D = 2;3$ ) extracted

from the wind tunnel tests from hot-wire anemometer measurement for the HK10 machine on a 1:10 scale. Due to the kinematic similarity between both flows, it is possible to compare the velocity profiles for operating conditions characterized by the dimensionless  $TSR = 1.6$ . See how the experimental and CFD results are very close in these profiles. Furthermore, it is also observed that in the wind tunnel, the effect of the velocity drop in the hub/nacelle region is not as pronounced as in the CFD-Full 3D.

On the other hand, the effect on the blade tip velocity ( $|z/D| \approx 0.5$ ) can be observed in the closest profiles ( $x/D = 1;2$ ), where the rotor geometry has a greater influence on the flow.

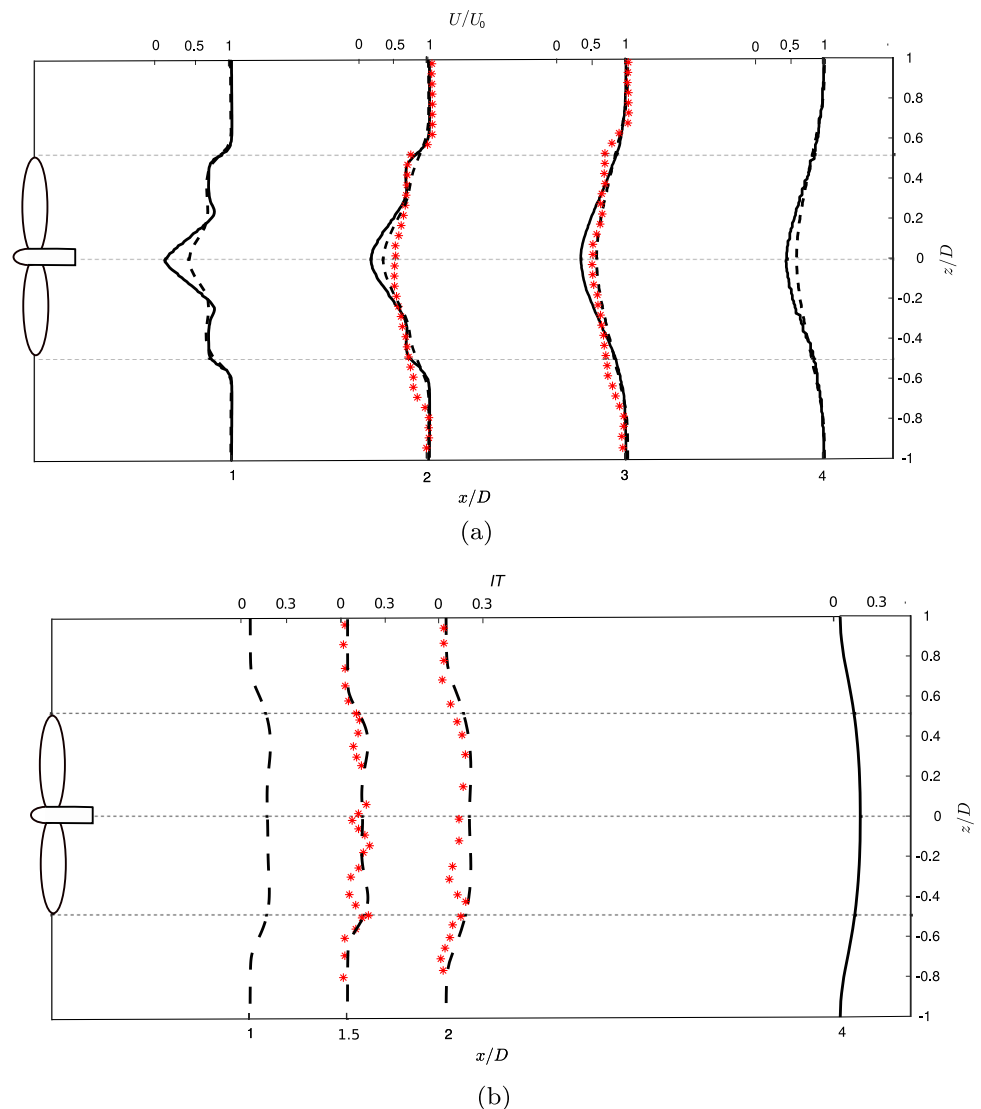
The profile  $X/D = 1.5$  presents two peaks coinciding with the blade tip regions, identifying the position of the blade tip vortex. Furthermore, it is observed how the values of turbulence intensity  $TI$  decrease as the flow develops and also how the disturbed area increases. In the position  $X/D = 1$ , this was limited to the rotor area, and in the case  $X/D = 4$  it goes even further. Both behaviors, also observed in the velocity profiles, are due to the phenomena of diffusion and mixing of the flow in the zones furthest from the wake due to the evolution of the flow.

In conclusion, the results between the simulations and the experiments have good adherence, reinforcing the quality of the integrated methodology using the different approaches to identify the main flow features in the wake. The velocity deficit in the wake is properly estimated, as well as the turbulence level. Therefore, the results presented for the HK10 rotor real machine operating in water flow show values and trends similar to those extracted from the wind tunnel tests for the scaled machine.

Finally, the mapping of the mean velocity and turbulence intensity for the plane  $x/D = 1.5$  is presented in Fig. 14 using the experimental data. In Fig. 14a, note that the flow, after crossing the rotor, presents a circular region, central to the rotor, with a large velocity deficit, as already observed in the profiles previously introduced. In addition, for the foreground, the influence of the tower on the flow is observed, delimited by the region of lower velocity.

In terms of the turbulence intensity, Fig. 14b shows the color map and Fig 14c the dimensionless energy density spectrum as a function of the dimensionless frequency by the optimal rotational speed,  $f/\omega$ , for the points indicated in the image, located in the center of the rotor and the blade tip of each plane. The high-intensity regions represent locations with large velocity fluctuations, which is eventually attributed to flow recirculation zones or even the presence of coherent structures. In the case described in Fig. 14b, the sectors of high turbulence intensity correspond to the blade tip and root vortices regions. It can be observed the angular distribution of small points with high intensity of turbulence around the turbine center, identifying the position of the

**Fig. 13** Transversal profiles. **a** Mean axial velocity and **b** turbulence intensity. (—) CFD-Full 3D (- -) CFD-ALM and (\*\*\*) Hot-wire measurements



blade tip vortex. Also, the hub/nacelle vortex's presence induces another great intensity region.

The signal spectra of the hot-wire measurements are shown in Fig. 14c, characterizing the typical bluff-body frequency distribution in the core region (2) and larger energy frequency distribution, close to the blade passage frequency (1). The tip vortex allows in the near-wake region a supplementary supplement of turbulence energy due to the size of the vortices in the large-scale range of the spectrum.

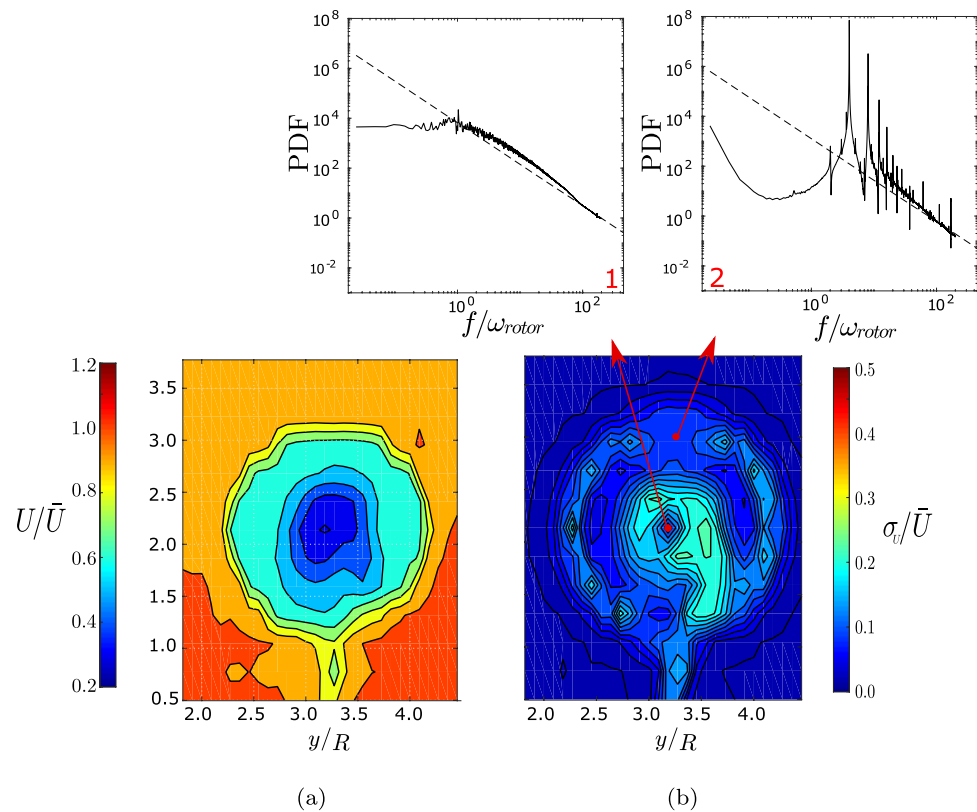
## 6 Conclusion

Two numerical approaches have predicted accurate results to describe the wake from the high-solidity turbine rotor in the nominal operating conditions. The profiles of mean and turbulent fields measured in the wind tunnel agree with the numerical simulation results in the near-wake positions. The

CFD-ALM approach was able to predict good results of the wake flow in this turbine, where the solidity is higher than in conventional three-blade wind turbines (the situation where the method has been developed). The simulation using the URANS approach with ALM is close to the CFD-Full 3D and to the experimental observations, predicting the dynamics of the vortex's structures, velocity and vorticity fields, velocity deficits in the wake, turbulence intensity, and its spectra. Also, the wake morphology was compared by means of the recognition of the tip/root vortices.

All main flow structures were predicted and confirmed by experiments using hot-wire measurements and PIV. The tip vortex allows an organized contribution in terms of the remaining energy after the hydrodynamical conversion in the rotating blades, with a large-scale characteristic. It is observed in the PIV experiments and in both numerical simulations, with equivalent hydrodynamical characteristics of its advected behavior. The hot-wire measurements identified

**Fig. 14** Cross-flow mapping from hot-wire measurements. **a** Mean axial velocity and **b** turbulence intensity. (1) and (2) show the spectra probability density function (PDF) in the mixing layer and in hub/nacelle shadowing vortices



the two different characteristic spectra for the hub and tip vortex effect. In the last condition, the energy amount close to the characteristic frequency of blade passage contributes mostly to the total energy of the fluctuating field. In the case of the core-shadowing region, the spectrum is equivalent to a conventional bluff-body flow. All these structures are alive downstream just at  $\sim 3.0D$  and it is broken by shear and turbulence, with an interaction with the core region and the smaller eddies. After that, a far-wake diffusion behavior is observed.

Results about the power coefficient  $C_p$  from CFD simulations and the experiments fit properly. The ALM  $C_p$  results show values close to experimental data around the nominal condition. The BEM in wind turbine aerodynamics has limitations that can lead to overestimation of aerodynamic performance. At high velocities, BEM assumes an attached boundary layer and neglects three-dimensional effects. This results in a simplified calculation of lift and drag coefficients based solely on the projected twisted angle, overlooking flow separation and non-uniformities in the boundary layer. Additionally, the neglect of three-dimensional effects disregards the radial flow gradients and spanwise distribution of aerodynamic forces. To improve accuracy, advanced models like computational fluid dynamics (CFD) should be employed to capture the complexities of the boundary layer and three-dimensional flow, especially at high wind speeds and tip speed ratios. Despite this, as mentioned, the numerical

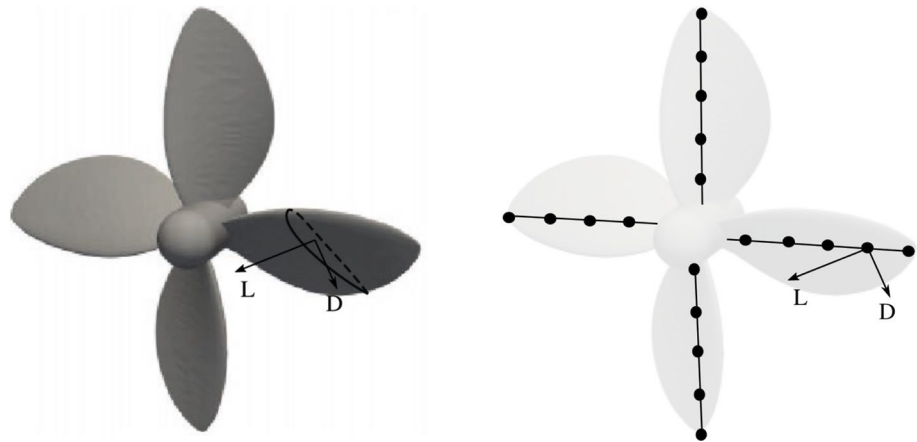
methods employed in this work can describe properly the wake flow in hydrokinetic rotors. In conclusion, the ALM technique can accurately depict the flow morphology in high-solidity horizontal-axis turbines, including structures like tip and root vortices. However, it tends to yield inaccurate estimates of the power coefficient. Conversely, the CFD-Full 3D approach, when fully utilized, can also capture the correct flow morphology and provide accurate  $C_p$  results. Nevertheless, it requires a higher number of mesh nodes and longer simulation times.

## Appendix

In this appendix, we describe the actuator line method [15] based on an iterative process, combining the blade element momentum (BEM) and CFD equations. The method solves the Navier–Stokes equations with a font term counting the hydrodynamic forces on the blades. Firstly, it computes the 2D hydrodynamic forces on the blades ( $\mathbf{f}_{2d}$ ). Later, it projects these forces in the field flow using a regularization Kernel function ( $\eta_e$ ) and incorporates the three-dimensional forces  $f_i(\mathbf{x})$  in the Navier–Stokes equations.

In the ALM method, the rotor is a set of ‘points’ or ‘elements’ along the axis of the blade, as in the scheme in Fig. 15; it is no longer used as a surface, bringing advantages

**Fig. 15** Full rotor geometry and blade discretization scheme to ALM. The hydrodynamic drag and lift forces,  $D$  and  $L$ , referred to any section of the blade are illustrated



such as lower computational costs or the possibility of structured mesh, suitable for large-eddy simulations.

The steps and main parameters to implement the ALM are described as:

1. *Rotor geometry definition:* Rotor is constituted of 4 blades and 2.2 m in diameter, and the hydrodynamic profile is a NACA 4415. Other geometric data for the design of the blades (radial distribution, chord, and torsion angle) were extracted from the Hydrok project and are summarized in Table 2.

For the ALM, the blades were discretized in 38 points, an estimated value based on the relationship proposed by [44] such that  $\Delta x = R/n$ , which relates the rotor radius,  $R = 1.1$  m, and the mesh element size,  $\Delta x = 0.03$  m, for the mesh presented in this work. In this way, it guarantees an appropriate relation between mesh size and blade discretization to prevent more than one point reside in the same mesh element.

2. *Turbine operating condition:* characterized by free stream velocity  $U_0 = 2.5$  m/s and rotational velocity  $\Omega = 35$  rpm, and, consequently, defined by tip speed ratio  $TSR = 1.6$ . After geometric and kinematic definition, Reynolds number is computed through the mean chord,  $c_m$ , and the relative flow velocity ( $U_{rel}$ ) at mean radial position  $R_m$ , to operation conditions, such as  $U_{rel} = \sqrt{U_0^2 + (\Omega R_m)^2}$ . Thus, the computed local Reynolds number is  $Re_L = 2 \times 10^6$ .
3. *Hydrofoil polar curves:* Using the free software XFOIL [45], which employs panel methods with a boundary layer formulation, the lift and drag coefficient,  $C_L(\alpha, Re_L)$  and  $C_D(\alpha, Re_L)$  as a function of angle of attack ( $\alpha$ ) and local Reynolds number, are computed and presented in Fig. 16. The input values to the software are the 2D hydrofoil geometry, the local Reynolds numbers, and the Mach number.
4. *Computing hydrodynamic forces by BEM method:* The two-dimensional hydrodynamic forces per unit length to each blade element are defined as

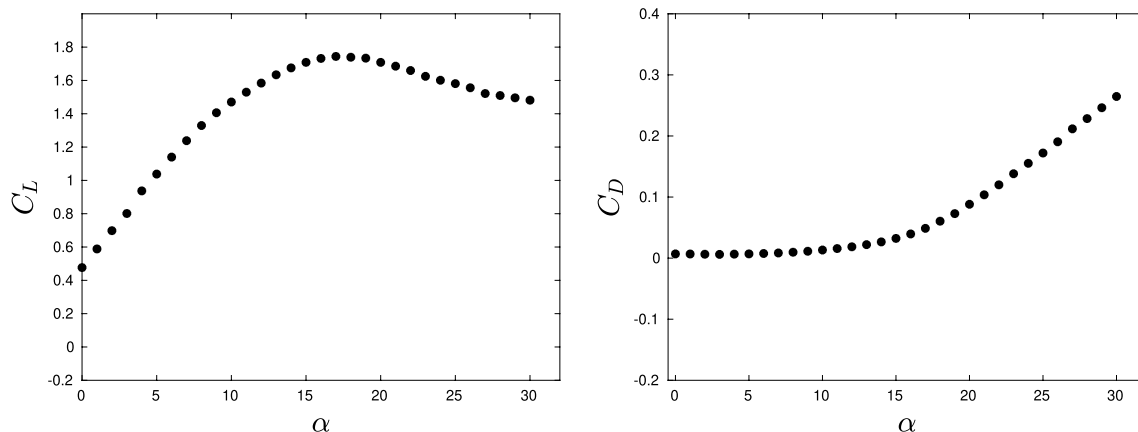


**Fig. 16** Lift ( $C_L$ ) and drag ( $C_D$ ) coefficient values of NACA4415 hydrofoil at various angles of attack ( $\alpha$ ) from XFOIL software [45]

$$\mathbf{f}_{2d} = f_L \mathbf{e}_L + f_D \mathbf{e}_D, \tag{4}$$

where  $f_L$  and  $f_D$  are calculated through equations 6 and 5, after to know the flow angle attack to each blade point, and to compute the relative flow velocity and the lift and drag coefficient.

$$f_D = \frac{1}{2} C_D(\alpha) \rho U_{rel}^2 c, \tag{5}$$

$$f_L = \frac{1}{2} C_L(\alpha) \rho U_{rel}^2 c, \tag{6}$$

where  $c$  is the chord length,  $\rho$  the flow density,  $U_{rel}$  the relative local velocity, and  $C_L$  and  $C_D$ , the lift and drag coefficients, respectively.

In each radial position and angle of attack, there is a specific value of the relative local velocity as well as  $C_L$  and  $C_D$ . So, the relative velocity is computed by

$$U_{rel} = \sqrt{U_z^2 + (\Omega r - U_\theta)^2}, \tag{7}$$

being  $U_z$  and  $U_\theta$  the axial and tangential velocities,  $\Omega$  the angular velocity and  $r$  the radius varying along the blade. On the other hand, the angle of attack is expressed as

$$\alpha = \Phi - \gamma, \tag{8}$$

where  $\Phi$  is the angle between the relative velocity and the rotor plane and,  $\gamma$  is the pitch angle, as observed in Fig. 17.

$$\Phi = \tan^{-1} \left( \frac{U_z}{\Omega r - U_\theta} \right). \tag{9}$$

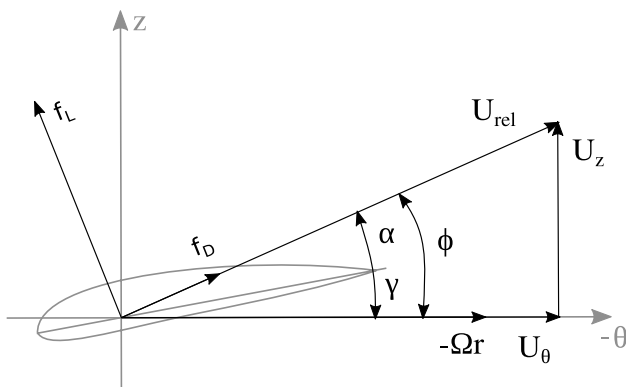


Fig. 17 Hydrofoil cross section illustrating the lift and drag hydrodynamic forces and the velocities triangle

5. *Projection of hydrodynamic forces (2D) to the flow field (3D):* computing the field flow,  $f_i$ , through the convolution integral of bi-dimensional forces and the kernel regularization function,  $\eta_\epsilon$ , such as

$$f_i(\mathbf{x}) = \sum_{k=1}^B \int_0^R F \mathbf{f}_{2D}(r) \cdot \mathbf{e}_i \eta_\epsilon(|\mathbf{x} - r\mathbf{e}_k|) dr, \tag{10}$$

where  $\mathbf{e}_k$  in the unit vector in the blade direction  $k$ ,  $|\mathbf{x} - r\mathbf{e}_k|$  is the distance between the mesh point and the actuator line point. The regularization function  $\eta_\epsilon$  is defined as

$$\eta_\epsilon(r) = \frac{1}{\epsilon^3 \pi^{3/2}} \exp[-(r/\epsilon)^2]. \tag{11}$$

The parameter  $\epsilon$  represents the reached kernel function and it is established as  $\Delta x \geq 2\epsilon$  [22, 46, 47]. Based on the mesh generated, the  $\epsilon$  value is defined as  $\epsilon = 2\Delta x = 0,06$ .

Finally, to highlight that the function  $F$  in Eq. 10 is the correction factor to tip blade effects developed by [48] such as

$$F = \frac{2}{\pi} \cos^{-1} \left[ \exp \left( -g \frac{B(R-r)}{2r \sin \Phi} \right) \right], \tag{12}$$

the parameter  $B$  refers to number of blades and the  $g$  coefficient depends of blade numbers,  $TSR$  value, chord distribution, pitch angle, etc... For simplicity, it established  $g$  to be only dependent on the blade numbers and the  $TSR$  [48], in the form

$$g = \exp(-c_1 (B\Omega R/U_\infty - c_2)), \tag{13}$$

being  $c_1$  e  $c_2$  coefficients estimated experimentally.

$$g = \exp(-0.125 (B\Omega R/U_\infty - 21)) + 0.1. \tag{14}$$

6. *Navier–Stokes equations solving:* the flow is solved inserting the field force  $f_i$  in Navier–Stokes equations,

$$\frac{\partial u_i}{\partial t} + u_j \frac{\partial u_i}{\partial x_j} = -\frac{1}{\rho} \frac{\partial p}{\partial x_i} + \nu \frac{\partial^2 u_i}{\partial x_j \partial x_j} + f_i. \tag{15}$$

After the velocity field is computed in the new time step, new angles of attack and relative velocities are defined turning to step 4, in an iterative process, where forces are computed and projected in the flow field again.

**Acknowledgements** This work was supported by the Brazilian funding agency CNPq (Ministry of Science, Technology and Innovation of Brazil) through Grant Nos. 310631/2021-1 and 408020/2022-9 and by FAPDF (Fundação de Apoio à Pesquisa do Distrito Federal)

through Grant No. 434/2022. Also, the authors acknowledge the support provided by Plan Propio-UCA 2022-2023 and Margarita Salas grant (NextGenerationEU) from the University of Cadiz. Finally, the authors thank the ENSAM-UnB cooperation program for aiding the experimental facilities and maintaining the research teams and their mobility.

## Declarations

**Conflict of interest** The authors declare that they have no conflict of interest.

## References

- Ibrahim WI, Mohamed MR, Ismail RM, Leung PK, Xing WW, Shah AA (2021) Hydrokinetic energy harnessing technologies: a review. *Energy Rep* 7:2021–2042
- Chaudhari S, Brown E, Quispe-Abad R, Moran E, Müller N, Pokhrel Y (2021) In-stream turbines for rethinking hydropower development in the Amazon basin. *Nat Sustain* 4(8):680–687
- Zhang W, Markfort CD, Porté-Agel F (2012) Near-wake flow structure downwind of a wind turbine in a turbulent boundary layer. *Exp Fluids* 52(5):1219–1235
- Lignarolo LEM, Ragni D, Krishnaswami C, Chen Q, Ferreira CJS, van Bussel GJW (2014) Experimental analysis of the wake of a horizontal-axis wind-turbine model. *Renew Energy* 70(Supplement C):31–46
- Bastankhah M, Porté-Agel F (2016) Experimental and theoretical study of wind turbine wakes in yawed conditions. *J Fluid Mech* 806:506–541
- Okulov VL, Naumov IN, Kabardin I, Mikkelsen R, Sørensen JN (2014) Experimental investigation of the wake behind a model of wind turbine in a water flume. *J Phys Conf Ser* 555(1):012080
- Macias MM, Mendes RCF, Oliveira TF, Brasil ACP (2020) On the upscaling approach to wind tunnel experiments of horizontal axis hydrokinetic turbines. *J Braz Soc Mech Sci Eng* 42:539
- Lust EE, Flack KA, Luznik L (2020) Survey of the near wake of an axial-flow hydrokinetic turbine in the presence of waves. *Renew Energy* 146:2199–2209
- Chamorro LP, Porté-Agel F (2009) A wind-tunnel investigation of wind-turbine wakes: boundary-Layer turbulence effects. *Bound-Layer Meteorol* 132(1):129–149
- Kang S, Kim Y, Lee J, Khosronejad A, Yang X (2022) Wake interactions of two horizontal axis tidal turbines in tandem. *Ocean Eng* 254:111331
- Toloui M, Chamorro LP, Hong J (2015) Detection of tip-vortex signatures behind a 2.5mw wind turbine. *J Wind Eng Ind Aerodyn* 143:105–112
- Nunes MM, Mendes RCF, Oliveira TF, Junior ACPB (2019) An experimental study on the diffuser-enhanced propeller hydrokinetic turbines. *Renew Energy* 133:840–848
- Silva PASF, De Oliveira TF, Brasil Junior AC, Vaz JR (2016) Numerical study of wake characteristics in a horizontal-axis hydrokinetic turbine. *Anais da Academia Brasileira de Ciencias* 88(4):2441–2456
- Howland MF, Bossuyt J, Martínez-Tossas LA, Meyers J, Meneveau C (2016) Wake structure in actuator disk models of wind turbines in yaw under uniform inflow conditions. *J Renew Sustain Energy* 8(4):043301
- Sørensen JN, Shen WZ (2002) Numerical modeling of wind turbine wakes. *J Fluids Eng* 124(2):393–399
- Kim T, Oh S, Yee K (2015) Improved actuator surface method for wind turbine application. *Renew Energy* 76:16–26
- Sandoval J, Soto-Rivas K, Gotelli C, Escarriaza C (2021) Modeling the wake dynamics of a marine hydrokinetic turbine using different actuator representations. *Ocean Eng* 222:108584
- Niebuhr CM, Schmidt S, van Dijk M, Smith L, Neary VS (2022) A review of commercial numerical modelling approaches for axial hydrokinetic turbine wake analysis in channel flow. *Renew Sustain Energy Rev* 158(2021):112151
- Li Z, Liu X, Yang X (2022) Review of turbine parameterization models for large-eddy simulation of wind turbine wakes. *Energies* 15(18):6533
- Baba-Ahmadi MH, Dong P (2017) Validation of the actuator line method for simulating flow through a horizontal axis tidal stream turbine by comparison with measurements. *Renew Energy* 113:420–427
- Baba-Ahmadi MH, Dong P (2017) Numerical simulations of wake characteristics of a horizontal axis tidal stream turbine using actuator line model. *Renew Energy* 113:669–678
- Yang X, Khosronejad A, Sotiropoulos F (2017) Large-eddy simulation of a hydrokinetic turbine mounted on an erodible bed. *Renew Energy* 113(July):1419–1433
- Baratchi F, Jeans TL, Gerber AG (2017) Actuator line simulation of a tidal turbine in straight and yawed flows. *Int J Mar Energy* 19:235–255
- Daskiran C, Riglin J, Oztekin A (2015) Computational study of multiple hydrokinetic turbines: the effect of wake. In: ASME international mechanical engineering congress and exposition proceedings (IMECE), no. November
- Liu C, Hu C (2019) An actuator line-immersed boundary method for simulation of multiple tidal turbines. *Renew Energy* 136:473–490
- Baratchi F, Jeans TL, Gerber AG (2019) A modified implementation of actuator line method for simulating ducted tidal turbines. *Ocean Eng* 193(October):106586
- Gorban AN, Gorlov AM, Silantyev VM (2001) Limits of the turbine efficiency for free fluid flow. *J Energy Resour Technol* 123(4):311–317
- Jump E, Macleod A, Wills T (2020) Review of tidal turbine wake modelling methods-state of the art. *Int Mar Energy J* 3(2):91–100
- El Fajri O, Bowman J, Bhushan S, Thompson D, O'Doherty T (2022) Numerical study of the effect of tip-speed ratio on hydrokinetic turbine wake recovery. *Renew Energy* 182:725–750
- Jackson RS, Amano R (2017) Experimental study and simulation of a small-scale horizontal-axis wind turbine. *J Energy Resour Technol Trans ASME* 139(5):1–19
- Porté-Agel F, Bastankhah M, Shamsoddin S (2020) Wind-turbine and wind-farm flows: a review, vol 174. Springer, Netherlands
- Mendes RC, Macías MM, Oliveira TF, Brasil AC (2021) A computational fluid dynamics investigation on the axial induction factor of a small horizontal axis wind turbine. *J Energy Resour Technol Trans ASME* 143(4):1–11
- Borg MG, Xiao Q, Allsop S, Incecik A, Peyrard C (2020) A numerical performance analysis of a ducted, high-solidity tidal turbine. *Renew Energy* 159:663–682
- Borg MG, Xiao Q, Allsop S, Incecik A, Peyrard C (2022) A numerical performance analysis of a ducted, high-solidity tidal turbine in yawed flow conditions. *Renew Energy* 193:179–194
- Zhang D, Guo P, Cheng Y, Hu Q, Li J (2023) Analysis of blockage correction methods for high-solidity hydrokinetic turbines: experimental and numerical investigations. *Ocean Eng* 283(March):115185
- Brasil ACP, Rafael J, Théo CFM, Ricardo W, Taygoara N (2019) On the design of propeller hydrokinetic turbines: the effect of the number of blades. *J Braz Soc Mech Sci Eng* 41(6):1–14



37. Hand MM, Sims DA, Fingersh LJ, Jager DW, Cotrell JR, Schreck S, Larwood SM (2001) Unsteady aerodynamics experiment phase vi: Wind tunnel test configurations and available data campaigns. Tech. rep., National Renewable Energy Lab., Golden, CO (US)
38. Massouh F, Dobrev I (2005) Investigation of wind turbine near wake (fluid machinery). In: The proceedings of the international conference on jets, wakes and separated flows (ICJWSF), pp 513–517
39. Ouro P, Dené P, Garcia-Novo P, Stallard T, Kyojuda Y, Stansby P (2023) Power density capacity of tidal stream turbine arrays with horizontal and vertical axis turbines. *J Ocean Eng Mar Energy* 9(2):203–218
40. Cruz LEB, Carmo BS (2020) Wind farm layout optimization based on CFD simulations. *J Braz Soc Mech Sci Eng* 42(8):433
41. Menter FR, Langtry R, Völker S (2006) Transition modelling for general purpose CFD codes. *Flow Turbul Combust* 77:277–303
42. Moshfeghi M, Song YJ, Xie YH (2012) Effects of near-wall grid spacing on sst-k- $\omega$  model using nrel phase vi horizontal axis wind turbine. *J Wind Eng Ind Aerodyn* 107:94–105
43. Sui C, Lee K, Huque Z, Kommalapati RR (2015) Transitional effect on turbulence model for wind turbine blade. In: ASME power conference, Vol. 56604, American Society of Mechanical Engineers, p. V001T11A006
44. Mikkelsen RF, Sørensen JN, Henningson DS, Andersen SJ, Ivanell S, Sarmast S (2015) Simulation of wind turbine wakes using the actuator line technique. *Philos Trans Royal Soc A Math Phys Eng Sci* 373(2035):20140071
45. Drela M (1989) XFOIL: an analysis and design system for low Reynolds number airfoilS. Spring-Verlag, New York
46. Martínez-Tossas LA, Churchfield MJ, Meneveau C (2015) Large Eddy simulation of wind turbine wakes: detailed comparisons of two codes focusing on effects of numerics and subgrid modeling. *J Phys Conf Ser* 625(1):1–10
47. Tzimas M, Prospathopoulos J (2016) Wind turbine rotor simulation using the actuator disk and actuator line methods. *J Phys Conf Ser*. <https://doi.org/10.1088/1742-6596/753/3/032056>
48. Shen WZ, Mikkelsen R, Sørensen JN, Bak C (2005) Tip loss corrections for wind turbine computations. *Wind Energy* 8(4):457–475

**Publisher's Note** Springer Nature remains neutral with regard to jurisdictional claims in published maps and institutional affiliations.

Springer Nature or its licensor (e.g. a society or other partner) holds exclusive rights to this article under a publishing agreement with the author(s) or other rightsholder(s); author self-archiving of the accepted manuscript version of this article is solely governed by the terms of such publishing agreement and applicable law.